Chinese Chemical Letters 37 (2026) 112529

Contents lists available at ScienceDirect

Chinese Chemical Letters

journal homepage: www.elsevier.com/locate/cclet

Steam-assisted Pt redispersion on SiO_2-supported CeO_2 enhances oxygen spillover for improved styrene catalytic oxidation

Yinye Chen[a], Huibin Cheng[b], Mingxian Gong[a], Kui Niu[a], Muping Shen[a], Yanqin Luo[a], Jiachang Zuo[a,*], Yuan Hu[c], Yongjin Luo[a,*], Qingrong Qian[a], Qinghua Chen[a]

[a] Digital Fujian Internet-of-things Laboratory of Environmental Monitoring, Fujian Key Laboratory of Pollution Control and Resource Reuse, College of Environmental and Resource Sciences, Fujian Normal University, Fuzhou 350117, China
[b] School of Civil Engineering, Fujian University of Technology, Fuzhou 350118, China
[c] College of Materials and Chemical Engineering, Minjiang University, Fuzhou 350108, China

ARTICLE INFO

Article history:
Received 10 September 2025
Revised 6 December 2025
Accepted 13 February 2026
Available online 13 February 2026

Keywords:
Catalytic styrene oxidation
High dispersion
Oxygen spillover
Active interface
Reaction mechanism

ABSTRACT

Metal-support active interfaces provide unique sites that enhance catalytic oxidation reactions. However, designing a catalyst that simultaneously promote both benzene ring cleavage and C–H bond scission remains a challenge. Herein, porous SiO_2 derived from waste rice husk was used to disperse CeO_2 nanoparticles, onto which Pt nanoparticles were deposited *via* ethylene glycol reflux reduction combined with steam redispersion to prepare a $Pt/CeO_2/SiO_2$ catalyst with abundant Pt–O–Ce active interfaces. Characterization and experimental results show that well-dispersed CeO_2 and Pt nanoparticles increase oxygen vacancy concentration and Pt–O–Ce interfaces, thereby enhancing oxygen spillover from CeO_2 to Pt and promoting styrene oxidation. The Pt–O–Ce interface accelerates the rate-determining C–H bond cleavage in benzaldehyde during styrene oxidation. $Pt/CeO_2/SiO_2$-H_2O catalyst with abundant oxygen vacancies and Pt–O–Ce interfaces achieves excellent catalytic performance (T_{90} = 222 °C, WHSV = 120,000 mL h^{-1} g^{-1}). Moreover, it demonstrates superior thermal stability over 40 h and water-resistance against 10 vol% H_2O, highlighting its industrial potential. This study offers a strategy for constructing supported catalysts with tailored active interfaces and high stability.

© 2026 Published by Elsevier B.V. on behalf of Chinese Chemical Society and Institute of Materia Medica, Chinese Academy of Medical Sciences.

Volatile organic compounds (VOCs) are key pollutants that degrade air quality [1–5]. Styrene (C_8H_8) is a typical malodorous VOCs, which is widely used in rubber production, paint manufacturing, and the plastics fabrication industries [6–8]. Studies have looked into the deterioration of C_8H_8 vapor in air. Catalytic oxidation is widely recognized as one of the most promising and efficient methods for styrene degradation among conventional approaches [9]. In practical industrial waste gas treatment environments, the water vapor content is uncontrollable, leading to competitive adsorption and blockage of the active sites on the catalyst. A key challenge lies in designing catalysts capable of simultaneously activating C–H bonds and cleaving the benzene ring in C_8H_8, while maintaining structural stability and water resistance under extreme conditions.

Developing high-performance catalysts relies on the accurate modulation of active sites and the refinement of reaction pathways. Extensive research has focused on constructing metal–support interfaces to achieve enhanced catalytic performance. Huang *et al.* [10] constructed a Pd–Si interface on ZSM-5 by regulating the electronic metal–support interaction (EMSI) between Pd and Si, improving formaldehyde degradation. Xiao *et al.* [11] discovered that the thermally driven interaction between Ni and adjacent Pt in $Pt/N\text{-}CeO_2$ catalysts leads to the formation of Pt–NiO interfaces, thereby enhancing toluene conversion. Juan *et al.* [12] synthesized a unique $Pd–iC–CeO_2$ interface through mechanical grinding, which promotes methane conversion. Such metal–support interfaces enable the transport of adsorbates or intermediates, a phenomenon known as spillover, such as hydrogen or oxygen species [13–15]. These interfaces not only facilitate the migration of reactive species, but also act as additional catalytic sites for O_2 activation, generating reactive oxygen species (*e.g.*, O_2^-, O^{2-}, O) and accelerating catalytic activity [16]. The spillover of oxygen species plays a crucial role in CO oxidation and VOCs degradation [17]. Chen *et al.* [18] regulated rutile-phase TiO_2 through tin doping, which activated the low-temperature reverse oxygen spillover process in the Pt/TiO_2 catalyst and thereby enhanced its CO oxidation activity. Wen *et al.* [19] found that Pt sites

* Corresponding authors.
E-mail addresses: zuo@fjnu.edu.cn (J. Zuo), yongjinluo@fjnu.edu.cn (Y. Luo).

https://doi.org/10.1016/j.cclet.2026.112529
1001-8417/© 2026 Published by Elsevier B.V. on behalf of Chinese Chemical Society and Institute of Materia Medica, Chinese Academy of Medical Sciences.

can activate gaseous oxygen, and the oxygen spillover from Pt sites to the MoO_3 surface significantly promotes the catalytic combustion of active hydrocarbons.

The Pt–O–Ce interface plays a critical role in regulating the adsorption and activation of reactants and intermediates on catalyst surfaces. Notably, the stability and dispersion of Pt species are key for efficient Pt–O–Ce interfaces, and steam treatment effectively regulates metal dispersion in supported catalysts. Nie *et al*. [20] showed steam maintains Pt^{2+} atomic dispersion in Pt/CeO_2, generates active surface lattice oxygen, and boosts low-temperature CO oxidation performance. Fan *et al*. [21] found steam induces Cu–OH formation and support hydroxyl enrichment, converting Cu nanoparticles to atomically dispersed Cu^{2+}. Pt demonstrates high activity for C–H bond cleavage [22,23], while CeO_2 exhibits exceptional oxygen storage-release capability [24–26]. Their synergy promotes rapid oxygen species migration and transformation at the interface, thereby accelerating VOCs oxidation [27]. Oxygen vacancies further optimize the local electronic structure of the Pt–O–Ce interface by modulating electron cloud distributions, enhancing the adsorption and conversion of reaction intermediates [28,29]. Xu *et al*. [30] prepared a Pt ALs/CeO_2 catalyst with abundant edge Pt–O–Ce active sites *via* a two-step calcination method, which involves epitaxial growth of small-sized atomic layer Pt on the CeO_2 surface. Wang *et al*. [31] prepared a high-loading and highly-dispersed Pt cluster catalyst of Pt_{AC}/CeO_2-O_v@GC, enriched with Pt–O–Ce structures *via* a molten salt electrochemical method, which enhances the oxygen reduction reaction. Recent efforts focus on anchoring single Pt atoms or clusters on CeO_2 nanoislands to prevent aggregation and maximize interfacial activity. Li *et al*. [32] anchored Pt atoms on CeO_x nanoislands of supported on porous silica, ensuring atomic dispersion under high-temperature with oxidative and reductive conditions. Chen *et al*. [33] confined Pt nanoclusters on CeO_x nanoislands and studied how the interaction between Pt clusters and single-atom Pt species influenced catalytic performance. However, the study of utilizing Pt–O–Ce active interfaces to promote the oxygen spillover from nanosized CeO_2 remains insufficient. On Pt-CeO_2 supported catalysts, oxygen transfer across the interface is a nanoscale phenomenon. Spillover occurs only on nanostructured or particulate CeO_2 in direct contact with Pt, and not on bulk or ordered CeO_2 [34–36].

Herein, porous SiO_2 derived from waste biomass rice husks was used to support uniformly dispersed CeO_2 nanoparticles. Subsequently, Pt nanoparticles were deposited onto the CeO_2/SiO_2 support *via* ethylene glycol reflux reduction combined with steam redispersion strategy, aiming to investigate the influence of synergistic effects among highly dispersed CeO_2, Pt nanoparticles, and SiO_2 on the formed Pt−O−Ce active interfaces. TEM, EPR, Raman, UV–vis, *in-situ* XPS, O_2-TPO, XANES, and *in-situ* DRIFTs reveal that the presence of CeO_2 and highly dispersed Pt nanoparticles increases oxygen vacancy concentration. Meanwhile, oxygen spillover from CeO_2 to Pt promotes the oxidation of C_8H_8. This work provides a pathway for designing catalysts with tailored active interfaces and provides insights into the preparation of highly stable catalysts.

The effect of the SiO_2 support and steam treatment on catalyst morphology was observed by SEM analysis. As shown in Fig. S1a (Supporting information), CeO_2/SiO_2 exhibits a clean, smooth and compact surface, suggesting that CeO_2 might penetrate into the porous structure of SiO_2. The morphology of the $Pt/CeO_2/SiO_2$ remains smooth and dense after Pt loading, indicating minimal structural disruption. In the absence of SiO_2 support, the particle size of Pt/CeO_2 (Fig. S1b in Supporting information) is larger than that of $Pt/CeO_2/SiO_2$ (Fig. S1c in Supporting information), likely due to the confinement effect of the SiO_2 porous framework, which promotes the formation of finely dispersed particles. After steam treatment, the morphology of $Pt/CeO_2/SiO_2$-H_2O (Fig. S1d in Supporting information) becomes loosely packed. This structural change may associate with the redispersion of Pt nanoparticles.

To explore the specific forms of CeO_2 and Pt species, TEM images of the catalysts were collected. As shown Fig. 1, the bright regions indicated by white arrows correspond to Pt nanoparticles. In Pt/CeO_2 (Fig. S2 in Supporting information), Pt nanoparticles exhibit aggregation with uneven distribution. In CeO_2/SiO_2 (Figs. S3a and b in Supporting information), CeO_2 nanoparticles are uniformly distributed on SiO_2 with an average particle size of 2 nm. After Pt loading, $Pt/CeO_2/SiO_2$ (Figs. 1a–d) displays aggregated Pt nanoparticles with an average size of 8 nm. After steam treatment, Pt nanoparticles are uniformly dispersed and the aggregates largely disappear for $Pt/CeO_2/SiO_2$-H_2O (Figs. 1e–h). The average particle size decreases from 8 nm to 3 nm, which is attributed to the hydroxyl groups generated during steam treatment promoting the formation of mobile Pt–OH species, thereby facilitating the breakup and migration of Pt nanoparticles [37–39]. EDX elemental mapping analysis further confirms the presence and uniform distribution of Pt and CeO_2 species [40], supporting the redispersion of Pt into small particles (Figs. S3c-d in Supporting information). CO pulse chemisorption measurements show Pt dispersions of 1.2 %, 13.9 %, and 17.8 % for Pt/CeO_2, $Pt/CeO_2/SiO_2$, and $Pt/CeO_2/SiO_2$-H_2O, respectively. This further verifies the improvement in dispersion. In addition, the actual Pt content in catalysts was tested by ICP-AES. As shown in Table S5 (Supporting information), the Pt contents in Pt/CeO_2, $Pt/CeO_2/SiO_2$, and $Pt/CeO_2/SiO_2$-H_2O are 0.9 %, 0.8 %, and 0.8 %, respectively.

XRD analysis demonstrated that the Pt peak at 39.7° characteristic of Pt particles disappears in steam-treated $Pt/CeO_2/SiO_2$-H_2O compared with $Pt/CeO_2/SiO_2$ (Fig. S4 in Supporting information), indicating enhanced Pt dispersion, consistent with the TEM results. UV–vis spectroscopy confirmed structural modifications in $Pt/CeO_2/SiO_2$-H_2O catalyst after steam treatment. The enhanced absorption at 400–600 nm (Fig. S5a in Supporting information) evidences CeO_2 defect formation induced by highly dispersed Pt nanoparticles with reduced particle sizes [41]. Moreover, the band gap narrowing from 3.08 eV to 3.00 eV (Fig. S5b in Supporting information) indicates increased Ce^{3+} species and oxygen vacancies, resulting from the partial Ce 4f orbitals filling, thereby enhancing visible-light absorption [42]. As shown in the EPR spectra (Fig. S6 in Supporting information), the peak at around $g = 2.003$ can be readily assigned to the oxygen vacancy [43,44]. Compared with the Pt/CeO_2, CeO_2, and Pt/SiO_2 catalysts, the $Pt/CeO_2/SiO_2$ catalyst exhibits significantly higher peak intensities of oxygen vacancies and Ce^{3+}. As expected, the $Pt/CeO_2/SiO_2$-H_2O catalyst shows even stronger peaks of oxygen vacancies and Ce^{3+} after steam treatment. These results indicate that the highly dispersed CeO_2 and Pt increase the oxygen vacancy concentration.

O_2-TPO analysis was employed to characterize the oxidation behavior and oxygen spillover over the catalysts. The experiment involved pre-reducing the catalyst in 10 % H_2/Ar, followed by exposure to 3 % O_2/He under programmed temperature ramping. By testing CeO_2/SiO_2 and Pt/SiO_2, the positions of the oxygen consumption peaks corresponding to the oxidation of Ce^{3+} to Ce^{4+} and that of Pt^0 to Pt^{2+} are distinguished. As shown in Fig. 1i, the peak at 331 °C in the CeO_2/SiO_2 catalyst represents the bulk re-oxidation of CeO_2 by gaseous O_2, which is an intrinsic property of the ceria support. By contrast, no obvious oxygen consumption peak was observed in Pt/SiO_2, as the oxidation of Pt^0 in this catalyst can only occur *via* the direct activation of gaseous O_2 on the Pt nanoparticles themselves. By comparison, besides the oxygen consumption peak appearing around 330 °C, $Pt/CeO_2/SiO_2$ and $Pt/CeO_2/SiO_2$-H_2O also showed an oxygen consumption peak around 450 °C. This indicates that the oxidation of Pt does not occur directly *via* gaseous O_2, but mainly relies on the active oxygen species spilled over from the CeO_2 support [45,46]. No-

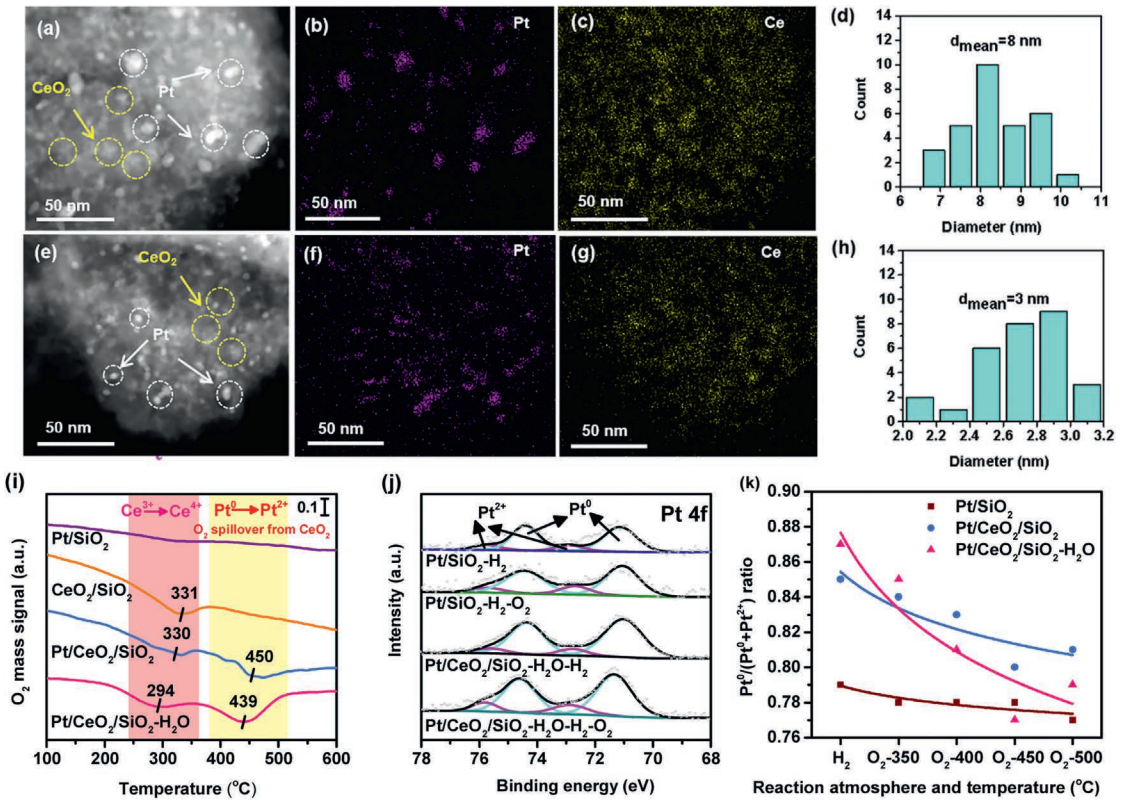


Fig. 1. (HR)TEM images, EDS elemental mapping, and Pt particle size distribution of (a–d) $Pt/CeO_2/SiO_2$ and (e–h) $Pt/CeO_2/SiO_2$-H_2O. (i) O_2-TPO profiles of Pt/SiO_2, CeO_2/SiO_2, $Pt/CeO_2/SiO_2$, and $Pt/CeO_2/SiO_2$-H_2O catalysts, (j) Pt 4f XPS spectra of Pt/SiO_2 and $Pt/CeO_2/SiO_2$-H_2O catalysts after H_2 reduction and O_2 oxidation, (k) plot of $Pt^0/(Pt^0+Pt^{2+})$ ratios for Pt/SiO_2, $Pt/CeO_2/SiO_2$, and $Pt/CeO_2/SiO_2$-H_2O catalysts in H_2 and O_2 (based on *quasi in situ* Pt 4f XPS spectra).

tably, the $Pt/SiO_2/SiO_2$-H_2O catalyst exhibits a large oxygen consumption peak at 439 °C, indicating a strong oxygen spillover effect. To further verify the occurrence of oxygen spillover, XPS was performed to analyze the valence state changes of Pt in Pt/SiO_2 and $Pt/SiO_2/SiO_2$-H_2O catalysts after reduction under 10 % H_2/Ar at 500 °C for 1 h or oxidation under 3 % O_2/He at 450 °C for 30 min (Fig. 1j). High-resolution Pt 4f XPS spectra show that Pt exists in both 0 and +2 oxidation states. For Pt/SiO_2, the $Pt^0/(Pt^0+Pt^{2+})$ ratios in Pt/SiO_2-H_2 (after H_2 reduction) and Pt/SiO_2-H_2-O_2 (after O_2 oxidation) are 0.83 and 0.80, respectively, with a minor difference of 0.03. By contrast, $Pt/CeO_2/SiO_2$-H_2O exhibits $Pt^0/(Pt^0+Pt^{2+})$ ratios of 0.89 (after H_2 reduction) and 0.82 (after O_2 oxidation), respectively, corresponding to a large difference of 0.07. This indicates that Pt in $Pt/CeO_2/SiO_2$-H_2O underwent a higher degree of oxidation, suggesting the involvement of spillover oxygen from CeO_2 to Pt in addition to gaseous O_2. Moreover, *quasi in-situ* XPS experiments were conducted to analyze the valence state changes of Pt in Pt/SiO_2, $Pt/SiO_2/SiO_2$, and $Pt/SiO_2/SiO_2$-H_2O after 10 % H_2/Ar reduction and 3 % O_2/He oxidation treatments at different temperatures (Fig. S7, Table S2 in Supporting information). Based on the Allometric1 plots presented in Fig. 1k, for Pt/SiO_2, the $Pt^0/(Pt^0+Pt^{2+})$ ratio showed only a minor change of 0.02 between H_2 reduction and O_2 oxidation, remaining almost unchanged across different oxidation temperatures. By contrast, $Pt/CeO_2/SiO_2$-H_2O, exhibited a ratio of 0.87 after reduction, decreasing to 0.85 after 350 °C oxidation and 0.77 after 450 °C oxidation, with a maximum difference achieving 0.1. For $Pt/CeO_2/SiO_2$, the $Pt^0/(Pt^0+Pt^{2+})$ ratio declines from 0.85 after reduction to 0.84 after oxidation at 350 °C, and 0.80 after oxidation at 450 °C, corresponding to a maximum change of 0.05, slightly lower than that of $Pt/CeO_2/SiO_2$-H_2O. This result further indicates that Pt in $Pt/CeO_2/SiO_2$-H_2O undergoes a higher degree of oxidation, consistent with the previous analysis.

CV measurement was employed to evaluate the electron transfer capability of catalysts over various voltage ranges (Fig. 2a), with electrochemical characterization conducted in a 0.25 mmol/L $K_3Fe(CN)_6$ solution [47]. Using CeO_2/SiO_2 and Pt/SiO_2 as control samples, the redox peak potential ranges of Pt and Ce species were determined. The CeO_2/SiO_2 catalyst exhibits redox pairs at 0.75 V and 0.63 V, ascribed to the redox reactions of Ce species. The Pt/SiO_2 catalyst shows redox pairs at 0.32 V and 0.22 V, associated with the redox transitions of Pt species. Within the voltage range of 0–0.8 V, electrochemical measurements revealed distinct redox behaviors for Pt/CeO_2, $Pt/CeO_2/SiO_2$, and $Pt/CeO_2/SiO_2$-H_2O catalysts. The $Pt/CeO_2/SiO_2$-H_2O catalyst exhibited the highest activity with oxidation/reduction peak currents of 39/57 μA for Pt species and 15/1.5 μA for Ce species, followed by $Pt/CeO_2/SiO_2$ (32/48 μA for Pt, 13/1 μA for Ce) and Pt/CeO_2 (29/45 μA for Pt, 12/2.5 μA for Ce). This indicates that greater numbers of Pt and Ce species participate in the redox reactions and more intense electron transfer occurring, thereby enhancing redox capabilities [48].

As observed in XANES spectra, the white line peak intensities of $Pt/CeO_2/SiO_2$-H_2O and $Pt/CeO_2/SiO_2$ are similar and fall between those of Pt foil and PtO_2. Moreover, its near-edge absorption energy is lower than that of PtO_2 (Fig. 2b). This indicates that the valence state of Pt is $\delta+$ ($0 < \delta < 4$), a phenomenon attributable to the partially unoccupied 5d orbitals of Pt [24,39], and is consistent with the XPS analysis. The coordination environment of platinum was characterized using Fourier transform extended X-ray absorption fine structure spectroscopy. As shown in Fig. 2c and Figs. S8a and b (Supporting information), the reference PtO_2 shows a prominent peak at ~1.6 Å, attributed to the Pt–O coordination. Both $Pt/CeO_2/SiO_2$ and $Pt/CeO_2/SiO_2$-H_2O catalysts exhibit a peak at ~2.5 Å, corresponding to Pt–Pt coordination, similar to that of Pt foil. Compared to the $Pt/CeO_2/SiO_2$ catalyst, the $Pt/CeO_2/SiO_2$-

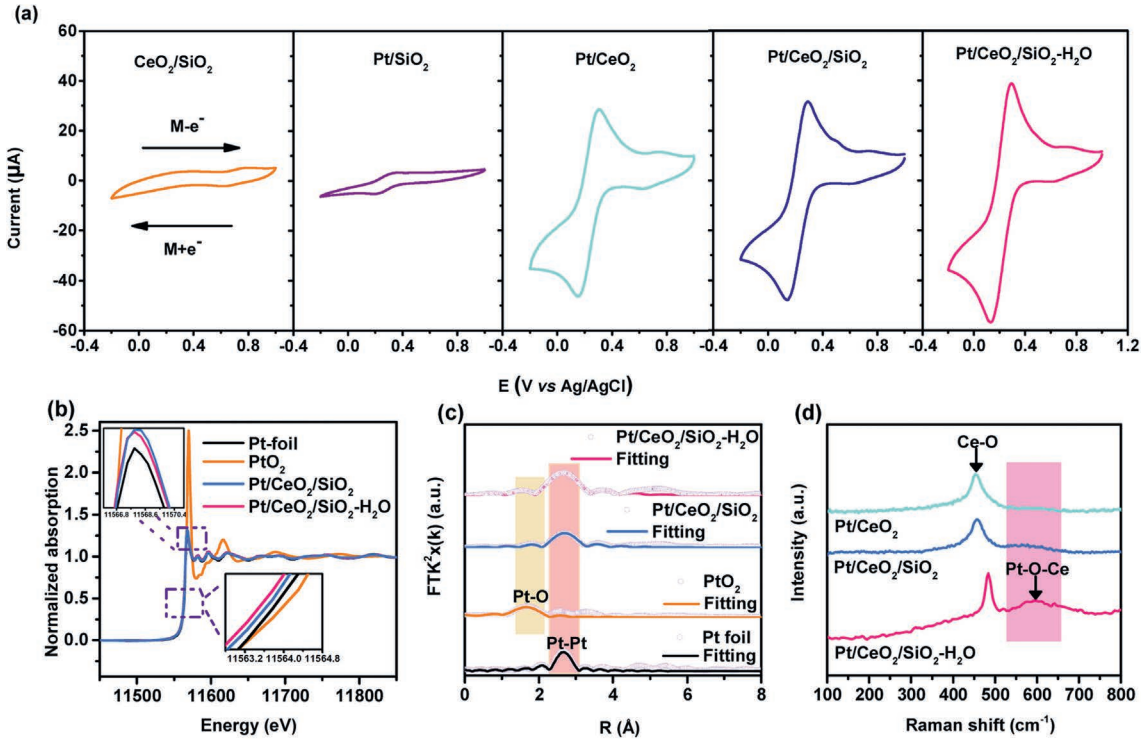


Fig. 2. (a) CV curves of Pt/SiO_2, CeO_2/SiO_2, $Pt/CeO_2/SiO_2$, and $Pt/CeO_2/SiO_2$-H_2O catalysts. (b, c) Normalized XANES and EXAFS magnitude of the Fourier transformed k^3-weighted $\chi(k)$ data for $Pt/CeO_2/SiO_2$ and $Pt/CeO_2/SiO_2$-H_2O at the Pt-L_3 edge. Pt foil and PtO_2 were used as reference. (d) Raman spectra of Pt/CeO_2, $Pt/CeO_2/SiO_2$, and $Pt/CeO_2/SiO_2$-H_2O catalysts.

H_2O catalyst exhibits a higher Pt–Pt bonding peak, suggesting a higher concentration of metallic Pt^0 in this catalyst (Table S3 in Supporting information). This observation is further supported by the wavelet transform analysis in Figs. S8c-f (Supporting information) [49,50].

Raman spectroscopy was conducted to clarify the atomic structure of catalysts. As evidenced by the Raman data in Fig. 2d, the distinctive F_{2g} phonon mode (463 cm^{-1}) associated with symmetric Ce–O bond stretching in cubic ceria units is present in all prepared catalysts. A weak band close to 570 cm^{-1} corresponding to the bridge Pt–O–Ce is indicated in the red rectangle [30]. This Pt–O–Ce band was observed exclusively in the $Pt/CeO_2/SiO_2$-H_2O catalyst, which may contribute to its good catalytic performance.

H_2-TPR analysis was conducted to examine the reduction behavior of the synthesized catalysts (Fig. S9 in Supporting information). CeO_2/SiO_2 shows reduction peaks at 280 °C and 700 °C, which are attributed to the reduction of surface CeO_2 and bulk CeO_2, respectively [51–53]. Pt/SiO_2 exhibits reduction peaks at 100 °C and 300 °C, corresponding to the reduction of Pt^{2+} to Pt^0 and the reduction related the Pt–O–Si interaction, respectively [30,54]. By contrast, Pt/CeO_2 and $Pt/CeO_2/SiO_2$ do not exhibit obvious reduction peaks corresponding to the conversion of Pt^{2+} to Pt^0. This may be attributed to the relatively large size of Pt nanoparticles, which makes their reduction more difficult. Compared with Pt/CeO_2, $Pt/CeO_2/SiO_2$ exhibits a higher surface CeO_2 reduction temperature. This may be because the small-sized CeO_2 particles are confined in the SiO_2 pores, which hinder their reduce. Notably, a reduction peak of Pt–O–Ce (115 °C) appears in $Pt/CeO_2/SiO_2$-H_2O [30], attributed to the uniform dispersion of small Pt particles after steam treatment, which facilitates the form a Pt–O–Ce interface with CeO_2.

To evaluate the catalytic activity, C_8H_8 was used as a model compound at 200 ppm concentration with a WHSV of 120,000 mL g^{-1} h^{-1}. The temperature-dependent C_8H_8 conversion profiles are depicted in Fig. 3a. The temperatures corresponding to 50 % and 90 % conversion (T_{50} and T_{90}), which serve as characteristic indicators of catalytic activity, are summarized in Table 1. Among the catalysts, Pt/CeO_2 exhibits the lowest activity, with T_{50} and T_{90} values of 229 °C and 269 °C, respectively. By contrast, $Pt/CeO_2/SiO_2$ shows significantly enhanced performance, with T_{50} and T_{90} reduced to 205 °C and 234 °C, respectively. This improvement may be attributed to the confinement effect of SiO_2, which reduces the sizes of Pt and CeO_2, thereby enhancing catalytic activity. Following steam treatment, the catalytic activity of $Pt/CeO_2/SiO_2$-H_2O is further enhanced, with T_{50} and T_{90} dropped to 190 °C and 222 °C, respectively. Additionally, the performance of Pt/SiO_2 was tested and found to exhibit low activity at low temperatures, indicating that highly dispersed CeO_2 is crucial for activating the styrene catalytic reaction. The CO_2 yield closely follows the C_8H_8 conversion (Fig. S10 in Supporting information), suggesting efficient deep oxidation capability. Comparison with reported high-performance catalysts (Fig. 3b and Table S4 in Supporting information) reveals that $Pt/CeO_2/SiO_2$-H_2O shows a high reaction rate of 29.28 μmol g^{-1} s^{-1} at 250 °C [9,42,55–59]. Given that industrial exhaust often contains steam, the influence of steam on catalytic activity was investigated. As shown in Fig. 3c, introducing 2 vol% and 5 vol% steam into the reaction stream system had negligible impact on the C_8H_8 conversion over $Pt/CeO_2/SiO_2$-H_2O. Even with 10 vol% steam, C_8H_8 conversion only decreased by 5 %, likely due to weakened competitive adsorption of H_2O at high temperatures [60]. Notably, the catalytic activity fully recovered shortly after steam removal, indicating excellent stability and steam resistance, and the potential for industrial applications.

To probe the intrinsic catalytic activity, kinetic measurements were conducted while maintaining C_8H_8 conversion below 15 %. A lower apparent activation energy (E_a) enables more reactant molecules to overcome the energy barrier and react, thereby accelerating the reaction. Based on the Arrhenius plots pre-

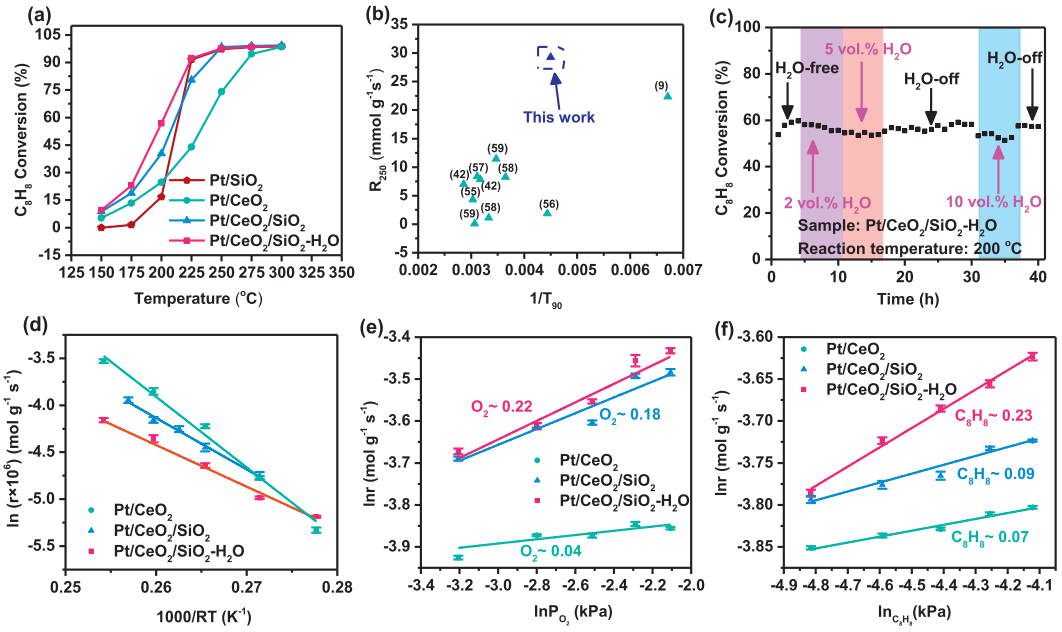


Fig. 3. (a) Evolution of the C_8H_8 conversion as the function of the reaction temperature. (b) Comparison with a variety of high-performance catalysts in the literature. (c) Stability of $Pt/CeO_2/SiO_2$-H_2O for C_8H_8 destruction under different humid conditions at 200 °C. (d) The E_a value over all catalysts, (e) reaction rate as a function of O_2 partial pressure, and (f) reaction rate as the function of C_8H_8 partial pressure.

Table 1
Comparison of catalytic performance, E_a, and TOF.

Catalyst	T_{50}[a] (°C)	T_{90}[b] (°C)	R_{200}[c] (μmol g^{-1} s^{-1})	S_{200}[d] (μmol m^{-2} s^{-1})	E_a (kJ/mol)	TOF[e] (s^{-1})
Pt/CeO_2	229	269	7	0.15	76 ± 4	0.7
$Pt/CeO_2/SiO_2$	205	234	12	0.04	57 ± 3	1.0
$Pt/CeO_2/SiO_2$-H_2O	190	222	19	0.07	45 ± 2	1.1

[a] The temperature required to reach a 50% conversion of C_8H_8.
[b] The temperature required to reach a 90% conversion of C_8H_8.
[c] C_8H_8 reaction rate at 200 °C.
[d] C_8H_8 specific reaction rate at 200 °C.
[e] Calculated at 200 °C. The amount of Pt is based on ICP-AES and CO pulse chemisorption.

sented in Fig. 3d, the E_a values of Pt/CeO_2, $Pt/CeO_2/SiO_2$, and $Pt/CeO_2/SiO_2$-H_2O are 76 ± 4, 57 ± 3, 45 ± 2 kJ/mol, respectively (Table 1). This indicates that C_8H_8 oxidation proceeds more readily over $Pt/CeO_2/SiO_2$-H_2O. This trend is consistent with the catalytic activity observed in the total oxidation of C_8H_8. Moreover, the turnover frequency (TOF) values based on Pt dispersion were calculated at 200 °C (Table 1). To further visualize this relationship, the TOF values were plotted against the Pt dispersion of the catalysts (Fig. S11 in Supporting information), revealing a clear linear increase in TOF with increasing Pt dispersion, and the $Pt/CeO_2/SiO_2$-H_2O catalyst reached a maximum value of 1.1 s^{-1}, indicating that enhanced Pt dispersion increased the number of Pt–O–Ce sites and facilitated the catalytic oxidation of C_8H_8. In summary, the superior performance of $Pt/CeO_2/SiO_2$-H_2O is primarily attributed to the synergistic effects of highly dispersed Pt nanoparticles, abundant oxygen vacancies, active Pt–O–Ce interfaces, and enhanced electron transfer capability, which collectively contribute to its exceptional catalytic performance.

Previous studies indicate that the catalytic oxidation reaction of C_8H_8 generally follows either the Mars-van Krevelen (MvK) mechanism or the Langmuir–Hinshelwood (L–H) mechanism. In the MvK mechanism, C_8H_8 molecules undergo a redox cycle on the catalyst surface by abstracting lattice oxygen, leading to oxidation of C_8H_8 and formation of oxygen vacancies. These oxygen vacancies are subsequently replenished by gas O_2 or the migration of lattice oxygen from the bulk, thereby restoring the catalyst to its initial state [24,61,62]. Under this mechanism, the reaction rate is insensitive to O_2 partial pressure. In order to analyze the reaction mechanism of C_8H_8, the reaction rates were measured at 170 °C under varying partial pressures of O_2 and C_8H_8 (Figs. 3e and f). For all catalysts, the reaction order of O_2 is below 1, supporting the MvK mechanism and indicating that lattice oxygen plays a major role in the reaction [63]. The reaction orders of C_8H_8 over Pt/CeO_2 and $Pt/CeO_2/SiO_2$-H_2O catalysts are 0.07 and 0.23 respectively, slightly higher than those of O_2 (0.04 and 0.22), indicating that these catalysts have a stronger adsorption capacity for C_8H_8 [64]. Therefore, the lattice oxygen in the catalysts can directly react with the adsorbed C_8H_8 *via* the MvK mechanism [65]. By contrast, the $Pt/CeO_2/SiO_2$ catalyst exhibits a higher reaction order for O_2 (0.18) than for C_8H_8 (0.09), suggesting that enhanced O_2 activation may facilitate the oxidation of C_8H_8. Furthermore, $Pt/CeO_2/SiO_2$-H_2O shows the highest reaction order for O_2 likely due to its elevated oxygen vacancy concentration.

Figs. S12a and b (Supporting information) display the pore size distribution and N_2 adsorption-desorption isotherms of the catalysts, respectively. In accordance with the IUPAC classification, these isotherms bear a resemblance to the standard type I adsorption-desorption isotherms, featuring an H1-type hysteresis loop. This characteristic indicates that mesopores are present in the catalysts. Table S5 presents the specific surface area, total pore volume, and average pore diameter of catalysts. Compared with Pt/CeO_2, the addition of SiO_2 carrier significantly increases the specific surface area while reducing the pore diameter.

XPS was implemented to investigate the electronic structure and surface elemental composition of catalysts. High-resolution Pt 4f spectra show that Pt exists predominantly in a mixture of the Pt^0 and Pt^{2+} species in all catalysts (Fig. S13 in Supporting information). Quantitative analysis (Table S6 in Supporting information) reveals that the $Pt^0/(Pt^0+Pt^{2+})$ ratio increases following the sequence of Pt/CeO_2 (0.78) < $Pt/CeO_2/SiO_2$ (0.82) < $Pt/CeO_2/SiO_2$-H_2O (0.85). This increase in Pt^0 content is likely one of the primary factors contributing to the excellent catalytic performance exhibited by $Pt/CeO_2/SiO_2$-H_2O. As demonstrated in Fig. S14a (Supporting information), the Ce 3d spectra can be deconvoluted into eight peaks, corresponding to four spin-orbit doublets associated with Ce^{3+} and Ce^{4+} [66]. Peaks V′, U′, U″, and U‴ are attributed to Ce^{3+}, while V, V″, V‴, and U correspond to Ce^{4+} [2]. Since Ce^{3+} is regarded as an indicator of oxygen vacancy formation, a high Ce^{3+} concentration implies more abundant oxygen vacancies [67–69]. The $Ce^{3+}/(Ce^{3+}+Ce^{4+})$ ratio for $Pt/CeO_2/SiO_2$-H_2O is 0.56, significantly higher than that of other catalysts (0.41–0.46), suggesting a high concentration of surface oxygen vacancies. Deconvolution of the O 1s spectra (Fig. S14b in Supporting information) yielded three components, which correspond to lattice oxygen (O_{latt}), adsorbed oxygen (O_{ads}), and surface hydroxyl (O_{OH}) at 531.1, 533.2, and 535.1 eV, respectively [70]. The ratio of $O_{ads}/(O_{latt}+O_{ads}+O_{OH})$ was utilized to assess the concentration of adsorbed oxygen species (presented in Table S6). $Pt/CeO_2/SiO_2$-H_2O catalyst exhibits the highest value of $O_{ads}/(O_{latt}+O_{ads}+O_{OH})$ indicating the highest concentration of adsorbed oxygen. O_2-TPD analysis was executed to gain a deeper understanding of the characteristics of surface oxygen species. As shown in Fig. S15 (Supporting information), the desorption peak below 300 °C is ascribed to oxygen species adsorbed on the surface in the vicinity of oxygen vacancies [42,71]. The peak area follows the sequence of $Pt/CeO_2/SiO_2$-H_2O > $Pt/CeO_2/SiO_2$ > Pt/CeO_2. The results indicate that $Pt/CeO_2/SiO_2$-H_2O contains a greater number of oxygen vacancies, thereby enabling it to adsorb a larger amount of surface-adsorbed oxygen species. This observation aligns with the results from UV–vis and Raman analyses.

The C_8H_8-TPD curves of catalysts are presented in Fig. S16 (Supporting information). For Pt/CeO_2, CO_2 peaks appear concurrently with the desorption of C_8H_8. This indicates that lattice oxygen species at surface defects oxidize a portion of C_8H_8 into CO_2. For $Pt/CeO_2/SiO_2$-H_2O, the significantly lower C_8H_8 desorption temperature (117 °C) suggests the presence of weak adsorption sites, where C_8H_8 molecules can desorb in a molecular form at low temperatures. More importantly, the much smaller C_8H_8 desorption peak area (3.2) coupled with the substantially larger CO_2 peak area (34.3) (Table S7 in Supporting information) clearly demonstrates its superior oxidation capability. The C_8H_8-TPSR profiles of catalysts are depicted in Fig. S17 and Table S7 (Supporting information). Within the temperature range of 70–200 °C, all catalysts exhibit similar C_8H_8 desorption behavior. This can be categorized as either strongly physically adsorbed or weakly chemically adsorbed C_8H_8. By contrast, the desorption peak area (4.1) of $Pt/CeO_2/SiO_2$-H_2O is relatively smaller. Along with the desorption of C_8H_8, a more intense CO_2 peak (Fig. S17b) emerges at approximately 300–400 °C. Subsequently, the broad CO_2 peaks between 450 and 600 °C arise from the oxidation of chemisorbed C_8H_8. The data suggests that the two prominent CO_2 generation peaks are associated with the interaction between adsorbed oxygen and surface lattice oxygen species. The CO_2 formation peak temperature of $Pt/CeO_2/SiO_2$-H_2O is lower compared to that of the other catalysts. This finding reveals that $Pt/CeO_2/SiO_2$-H_2O exhibits superior oxygen mobility, which promotes oxidation activity.

The complex C_8H_8 oxidation process was investigated through *in situ* DRIFTS. As displayed in Fig. 4, the band at 3060 cm^{-1} corresponds to the C–H stretching vibration of adsorbed C_8H_8, and the bands at 1572 and 1622 cm^{-1} are attributed to the typical aromatic ring vibrations, implying the adsorption of C_8H_8 on all catalysts. In addition, the intermediates of C_8H_8 degradation were also detected. The band at around 1335 cm^{-1} is probably ascribed to the C–O stretching vibration of benzyl alcohol, formed through the oxidative cleavage of the C_8H_8 double bon. The bands observed at 1717 cm^{-1} is due to the formation of the C=O group in benzaldehyde while the band at 1504, 1521, and 1399 cm^{-1} are assigned to benzoic acid. Moreover, the bands located at 1427 and 1215 cm^{-1} can be identified as maleic anhydride, indicating the ring-breakage of phenyl. It can be seen from Fig. 4a that with the increase in the temperature of the oxidation reaction, there is no significant change in the intermediate products of Pt/CeO_2, indicating that the oxidation ability of Pt/CeO_2 is relatively weak. For $Pt/CeO_2/SiO_2$ (Fig. 4b), there was no significant change in the intermediate products before 180 °C. After the temperature was raised to 230 °C, the C–H vibration peak of C_8H_8 at 3060 cm^{-1} became weaker, while the peak intensity of CO_2 (2350 cm^{-1}) increased. When the temperature reached 250 °C, the C–H vibration peak of C_8H_8 decreased significantly. Except for the peak of benzyl alcohol becoming smaller, the vibration peaks of the other intermediate products such as benzaldehyde, benzoic acid, and maleic anhydride all became stronger. With the increase in the reaction temperature of $Pt/CeO_2/SiO_2$-H_2O (Fig. 4c), the peak intensities of the C–H vibration peak of C_8H_8 and that of benzyl alcohol gradually decreased, while the peaks of benzaldehyde and CO_2 gradually increased. The peak of benzyl alcohol reaches a maximum at 180 °C and decreases as the temperature rises to 230 °C. At 250 °C, the benzaldehyde peak decreases significantly and is lower than that of $Pt/CeO_2/SiO_2$, indicating that $Pt/CeO_2/SiO_2$-H_2O has a stronger oxidation capacity. The cleavage of benzaldehyde is the key rate-determining step in C_8H_8 oxidation, and the existence of Pt–O–Ce active sites facilitates benzene ring cleavage in benzaldehyde.

Combined with *in situ* DRIFTS, Raman, H_2-TPR, *quasi in situ* XPS, and O_2-TPO analyses, the reaction mechanism for the oxidation of C_8H_8 over $Pt/CeO_2/SiO_2$ and $Pt/CeO_2/SiO_2$-H_2O can be outlined as follows: Styrene (C_8H_8) → benzyl alcohol (C_7H_8O) → benzaldehyde (C_7H_6O) → benzoate (C_6H_5COOH) → maleates ($C_4H_4O_4$) → carbon dioxide and water (CO_2, H_2O) (Fig. 5) [9,42,47]. For Pt/CeO_2, only benzoic acid and maleic acid were detected as intermediate products, reflecting its poor oxygen mobility and weak oxidation capacity.

To analyze the influence of oxygen spillover on the deep oxidation of styrene, the styrene oxidation processes of the Pt/SiO_2, $Pt/CeO_2/SiO_2$, and $Pt/CeO_2/SiO_2$-H_2O catalysts were investigated after reduction in 10 % H_2/Ar (30 mL/min) at 230 °C and subsequent oxidation in 3 % O_2/He (30 mL/min) at different temperatures. For Pt/SiO_2 (Fig. 4d), the characteristic peaks of the styrene oxidation products remained basically consistent after H_2 reduction and O_2 oxidation at different temperatures. By contrast, for $Pt/CeO_2/SiO_2$ (Fig. 4e), the C=O vibration peak of benzaldehyde at 1717 cm^{-1} was significantly enhanced after oxidation at 450 °C, indicating that the oxygen spillover of CeO_2 promoted the oxidation of styrene. Notably, for $Pt/CeO_2/SiO_2$-H_2O (Fig. 4f), both the C=O vibration peak of benzaldehyde at 1717 cm^{-1} and the CO_2 peaks significantly enhanced, exceeding the intensities observed for $Pt/CeO_2/SiO_2$. This suggests that $Pt/CeO_2/SiO_2$-H_2O has a stronger oxygen spillover and enhanced capacity for C_8H_8 deep oxidation.

Herein, the confinement effect of waste rice husk-derived porous SiO_2 was used to fabricate highly uniform CeO_2. Then, highly dispersed Pt nanoparticles were deposited on CeO_2/SiO_2 *via* a strategy combining ethylene glycol reflux reduction and steam redispersion. Steam treatment promoted the redispersion of Pt aggregates into fine Pt nanoparticles at low temperature, while the resulting highly dispersed CeO_2 and Pt nanoparticles increase the oxygen vacancy concentration. Pt–O–Ce active interfaces promote

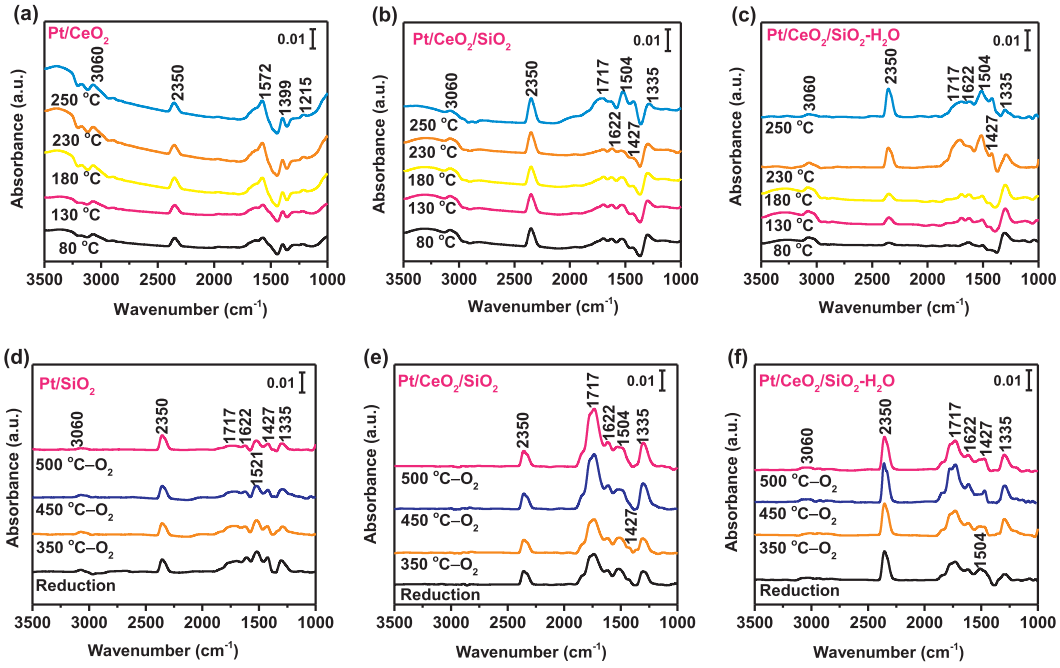


Fig. 4. *In situ* DRIFTS of styrene degradation collected over (a) Pt/CeO_2, (b) $Pt/CeO_2/SiO_2$, and (c) $Pt/CeO_2/SiO_2$-H_2O. *In situ* DRIFTS of styrene degradation over catalysts after H_2 reduction and O_2 oxidation: (d) Pt/SiO_2, (e) $Pt/CeO_2/SiO_2$, and (f) $Pt/CeO_2/SiO_2$-H_2O.

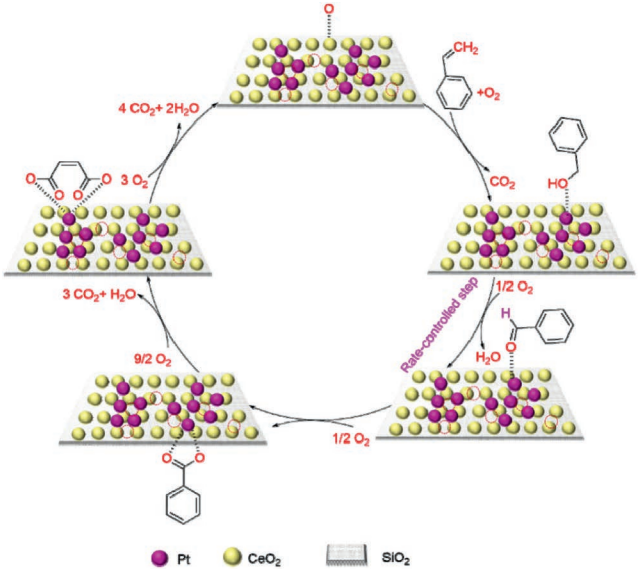


Fig. 5. Proposed reaction pathway for the catalytic degradation of styrene over $Pt/CeO_2/SiO_2$-H_2O catalyst.

the oxygen spillover from CeO_2 nanoparticles to Pt and facilitates the catalytic oxidation of C_8H_8 over $Pt/CeO_2/SiO_2$-H_2O catalyst. The Pt–O–Ce interface induced C-H bond cleavage in benzaldehyde is the rate determining step of C_8H_8 oxidation. $Pt/CeO_2/SiO_2$-H_2O exhibited the highest catalytic oxidation activity for C_8H_8 (T_{90} = 222 °C, WHSV=120,000 mL h^{-1} g^{-1}). Additionally, it showed favorable thermal stability and resistance to steam (10 vol%). This study proposes a strategy for fabricating supported catalysts that possess specific active interfaces and high stability.

CRediT authorship contribution statement

Yinye Chen: Writing – original draft, Methodology, Investigation, Data curation, Conceptualization. **Huibin Cheng:** Investigation, Data curation. **Mingxian Gong:** Writing – review & editing, Validation. **Kui Niu:** Visualization, Validation. **Muping Shen:** Validation. **Yanqin Luo:** Validation. **Jiachang Zuo:** Writing – review & editing, Resources. **Yuan Hu:** Methodology. **Yongjin Luo:** Writing – review & editing, Funding acquisition. **Qingrong Qian:** Resources, Funding acquisition. **Qinghua Chen:** Resources, Funding acquisition.

Declaration of competing interest

The authors declare that they have no known competing financial interests or personal relationships that could have appeared to influence the work reported in this paper.

Acknowledgments

This work was financially supported by the National Natural Science Foundation of China (No. 22478072), National Key Research and Development Program of China (No. 2023YFC3906300), and Young Top Talents of Fujian Young Eagle Program.

Supplementary materials

Supplementary material associated with this article can be found, in the online version, at doi:10.1016/j.cclet.2026.112529.

References

[1] Y. Zheng, Q. Liu, C. Shan, et al., Environ. Sci. Technol. 55 (2021) 5403–5411.
[2] S. Mo, J. Li, R. Liao, et al., Chem. Eng. J. 418 (2021) 129399.
[3] J. Kong, S. Song, W. Zhao, et al., Appl. Catal. B 339 (2023) 123118.
[4] P. Wang, X. Ma, X. Hao, et al., Catal. Rev. 66 (2022) 586–639.
[5] H. Zhang, Z. Wang, L. Wei, et al., Chin. J. Catal. 61 (2024) 71–96.
[6] J. Shi, J. Chen, G. Li, et al., Catal. Today 281 (2017) 621–629.
[7] J. Chen, Z. He, Y. Ji, et al., Appl. Catal. B 257 (2019) 117912.
[8] J. Wu, J. Wang, C. Liu, et al., Environ. Sci. Technol. 56 (2022) 13996–14007.
[9] Y. Zhang, W. Zhu, J. Lu, et al., Appl. Catal. B 342 (2024) 123461.
[10] T. Dong, J. Ji, L. Yu, et al., JACS Au 3 (2023) 1230–1240.
[11] M. Xiao, D. Han, X. Yang, et al., Appl. Catal. B 323 (2023) 122173.
[12] J. Jiménez, P. Lustemberg, M. Danielis, et al., J. Am. Chem. Soc. 146 (2024) 25986–25999.

[13] Y. Yang, W. Zheng, P. Wang, et al., ACS Nano 18 (2024) 24458–24468.
[14] E. Lee, S. Kang, A. Beck, et al., ACS Catal. 15 (2025) 9477–9488.
[15] Y. Zhu, F. Guo, Q. Wei, et al., Adv. Funct. Mater. 35 (2025) 2421354.
[16] D. Shen, F. Sun, Z. Liang, et al., Nat. Commun. 16 (2025) 3883.
[17] M. Gao, Z. Yang, H. Zhang, et al., ACS Cent. Sci. 8 (2022) 1633–1645.
[18] J. Chen, S. Xiong, H. Liu, et al., Nat. Commun. 14 (2023) 3433.
[19] C. Wen, L. Xu, Y. Hao, et al., ACS Catal. 15 (2025) 10746–10757.
[20] L. Nie, D. Mei, H. Xiong, et al., Science 363 (2019) 1419–1423.
[21] Y. Fan, R.T. Li, B.B. Wang, et al., Nat. Commun. 15 (2024) 3046.
[22] B. Liu, F. Wang, X. Dou, et al., Sci. China Chem. 67 (2024) 1017–1027.
[23] M. Song, R. Zhang, B. Zhang, et al., Appl. Catal. B 363 (2025) 124787.
[24] V. Muravev, A. Parastaev, Y. van den Bosch, et al., Science 380 (2023) 1174–1179.
[25] Y. Ma, B. Chi, W. Liu, et al., ACS Catal. 9 (2019) 8404–8412.
[26] K. Khivantsev, H. Pham, M.H. Engelhard, et al., Nature 640 (2025) 947–953.
[27] Y. Ren, C. Song, H. Wang, et al., ACS Catal. 14 (2024) 4340–4351.
[28] W. Yang, F. Qi, W. An, et al., ACS Catal. 14 (2024) 5936–5948.
[29] L. Borges, A. Braga, D. Zanchet, et al., Appl. Catal. B 325 (2023) 122361.
[30] A. Xu, T. Liu, D. Liu, et al., Angew. Chem. Int. Ed. 63 (2024) e202410545.
[31] C. Fan, S. Dou, X. Zhan, et al., Nano Lett. 24 (2024) 6957–6964.
[32] X. Li, X.I. Pereira-Hernández, Y. Chen, et al., Nature 611 (2022) 284–288.
[33] Y. Chen, J. Zhao, X. Zhao, et al., Nat. Chem. Eng. 2 (2025) 38–49.
[34] T. Bunluesin, R.J. Gorte, G.W. Graham, Appl. Catal. B 15 (1998) 107–114.
[35] G. Vayssilov, Y. Lykhach, A. Migani, et al., Nat. Mater. 10 (2011) 310–315.
[36] Z. Yan, X. Wang, Y. Zhang, et al., Appl. Catal. B 358 (2024) 124389.
[37] Y. Yang, X. Bie, X. Qi, et al., ACS Catal. 15 (2025) 5847–5857.
[38] H. Lei, N. Zhang, S. Hu, et al., Angew. Chem. Int. Ed. 64 (2025) e202509239.
[39] R. Aunkon, H. Choi, R. Shimogawa, et al., ACS Catal. 15 (2025) 19709–19720.
[40] J. Lei, Z. Wu, D. Ye, et al., Angew. Chem. Int. Ed. 64 (2025) e202511913.
[41] N. Acerbi, S. Golunski, S.C. Tsang, et al., J. Phys. Chem. C 116 (2012) 13569–13583.
[42] Y. Zhang, J. Lu, L. Zhang, et al., Appl. Catal. B 309 (2022) 121249.
[43] Y. Chong, T. Chen, B. Zhou, et al., ACS Catal. 14 (2024) 7201–7212.
[44] J. Zhang, Y. Yang, F. Qin, et al., Adv. Healthc. Mater. 12 (2023) 2302056.
[45] F. Noronha, E. Fendley, R. Soares, et al., Chem. Eng. J. 82 (2001) 21–31.
[46] S. Stagg-Williams, F. Noronha, G. Fendley, et al., J. Catal. 194 (2000) 240–249.
[47] Y. Lin, X. Wang, W. Lan, et al., Ind. Eng. Chem. Res. 64 (2025) 7313–7324.
[48] Y. Zhang, J. Wu, T. Li, et al., ACS Catal. 14 (2024) 1706–1713.
[49] H. Funke, A.C. Scheinost, M. Chukalina, Phys. Rev. B 71 (2005) 094110.
[50] R. Savinellia, S. Scott, Phys. Chem. Chem. Phys. 12 (2010) 5502–5502.
[51] L. Nie, D. Mei, H. Xiong, et al., Science 363 (2019) eaaw5872.
[52] J. Lee, Y. Ryou, X. Chan, et al., J. Phys. Chem. C 120 (2016) 25870–25879.
[53] J. Yu, X. Qin, Y. Yang, et al., J. Am. Chem. Soc. 146 (2023) 1071–1080.
[54] Y. Li, T. Qin, H. Guo, et al., Nano Res. 18 (2025) 94907431.
[55] T. Fu, Y. Zhang, D. Wu, et al., J. Hazard. Mater. 397 (2020) 122630.
[56] J. Kong, Z. Xiang, G. Li, et al., Appl. Catal. B 269 (2020) 118755.
[57] G. Xiao, S. Xin, H. Wang, et al., Ind. Eng. Chem. Res. 58 (2019) 5388–5396.
[58] Y. Chen, Z. Zhang, X. Wang, et al., ACS Appl. Mater. Interfaces 15 (2023) 32404–32415.
[59] Y. Chen, C. Cao, C. Huang, et al., Appl. Surf. Sci. 606 (2022) 154851.
[60] F. Bi, X. Zhang, J. Chen, et al., Appl. Catal. B 269 (2020) 118767.
[61] N. Zhang, J. Zhao, J. Wei, et al., Nano Lett. 25 (2025) 4046–4053.
[62] L. Wang, S. Deo, A. Mukhopadhyay, et al., ACS Catal. 12 (2022) 12927–12941.
[63] Y. Luo, Y. Zheng, X. Feng, et al., ACS Appl. Mater. Interfaces 12 (2020) 23789–23799.
[64] X. Liu, Y. Shi, L. Yu, et al., Environ. Sci. Technol. 59 (2025) 6331–6340.
[65] T. Gan, X. Chen, X. Chu, et al., J. Am. Chem. Soc. 146 (2024) 16549–16557.
[66] J. Du, Z. Qu, C. Dong, et al., Appl. Surf. Sci. 433 (2018) 1025–1035.
[67] N. Feng, Z. Zhu, P. Zhao, et al., Appl. Surf. Sci. 515 (2020) 146013.
[68] K.A. Resende, A.H. Braga, F.B. Noronha, et al., Appl. Catal. B 245 (2019) 100–113.
[69] W. She, T. Qi, M. Cui, et al., ACS Appl. Mater. Interfaces 10 (2018) 17487–17487.
[70] Y. Feng, C. Wang, C. Wang, et al., J. Hazard. Mater. 424 (2022) 127337.
[71] Y. Ma, L. Wang, J. Ma, et al., ACS Catal. 11 (2021) 6614–6625.